Frontiers of Optoelectronics (2026) 19:22
https://doi.org/10.2738/foe.2026.0022

Frontiers of Optoelectronics

RESEARCH ARTICLE

Nanoprecision real-time diameter control of micro/nanofibers via higher-order mode interference

Dezhou Lu[1*] · Hao Chi[1*] · Liying Chen[1] · Mengyang Jin[1] · Jiahui Wu[1] · Zhuning Wang[1] · Yaoguang Ma (✉)[1]

Received: 4 November 2025 / Accepted: 3 April 2026

Abstract

In this paper, we report a mode-interference-based approach for the efficient and reliable diameter measurement of micro/nanofibers (MNFs), enabling the *in situ* monitoring of MNFs fabricated from both single-mode fibers (SMFs) and multimode fibers (MMFs). The proposed method integrates automated signal processing with parameter-corrected flame-brush models, establishing a real-time closed-loop feedback mechanism during the fabrication process. Within the 524–1778 nm range, measurement accuracies better than 8 nm (< 1.25%) for SMF and 5 nm (< 0.78%) for MMF are demonstrated. Furthermore, to address the challenge of reconstructing complex taper profiles, we introduce a one-dimensional convolutional neural network (1D-CNN). Trained on a physics-enhanced data set, this network enables the end-to-end precision measurement of taper morphology. Within the diameter range of 1.9–10 μm, the maximum relative error is maintained below 0.35%, with a maximum absolute error of less than 9 nm. This method demonstrates broad applicability, offering a reliable solution for the fabrication of high-performance MNF-based photonic devices.

Keywords Micro/nanofiber · Short-time Fourier transform · Deep learning · 1D-CNN · Full-profile measurement.

1 Introduction

By heating and softening a standard optical fiber with high temperature and stretching it from both ends, a micro/nanofiber (MNF) with gradually reduced diameter at both ends and the thinnest section in the middle, where the diameter is typically on the order of the wavelength, can be produced. Depending on the morphological profile of the taper transition region, MNFs are primarily classified into adiabatic and non-adiabatic types, each exhibiting unique advantages in distinct applications. Specifically, featuring ultralow transmission loss and strong optical confinement [1–3], adiabatic MNFs are extensively utilized in dispersion compensation [4,5], supercontinuum generation [6–8], quantum optics [9,10]. In contrast, non-adiabatic MNFs excite multimode coupling and interference through their relatively steep taper profiles [11,12]. This strong modal interaction renders them highly sensitive to variations in the ambient refractive index and structural morphology, making them pivotal in the development of various high-precision optical sensors [13–15] and spectrometer [16].

The optical properties of MNFs are highly sensitive to nanometer-scale shape variations. Different applications require MNFs with tailored geometries. With the growing industrial need for precise control over optical fields, it becomes increasingly vital to precisely fabricate MNFs with diverse shapes and enable real-time diameter feedback. For example, in composite crystal microcavity systems, the waist diameter of the MNF governs the phase-matching conditions for specific resonant wavelengths [17,18]. In cold atom trapping applications, precise tuning of the fiber diameter optimizes the evanescent field distribution, which improves the atom-light coupling efficiency and increases the number of trapped atoms [19,20]. Furthermore, in the realm of nonlinear optics, tailoring the fiber diameter to achieve an appropriate effective mode area is essential for realizing efficient nonlinear frequency conversion [21].

While existing measurement techniques have demon-

*Dezhou Lu and Hao Chi contributed equally to the work.

✉ Yaoguang Ma
mayaoguang@zju.edu.cn

[1] State Key Laboratory for Extreme Photonics and Instrumentation, College of Optical Science and Engineering, Intelligent Optics and Photonics Research Center, ZJU–Hangzhou Global Scientific and Technological Innovation Center, International Research Center for Advanced Photonics, Zhejiang University, Hangzhou 310027, China

strated high precision in specific scenarios, achieving rapid and precise characterization of MNF profiles remains a significant challenge. For instance, techniques based on standing-wave illumination [22] require intricate alignment systems, whereas methods utilizing coherent forward stimulated Brillouin scattering [23] or propagation constants [24] depend on costly detection instrumentation. Although Monte Carlo simulations [25] provide comprehensive theoretical models, they are computationally intensive. Conversely, methods employing high-sensitivity photodetectors [26] or scattering loss analysis [27] offer experimental simplicity and rapid response but are highly susceptible to environmental disturbances. Consequently, there is a critical need to develop a measurement scheme that simultaneously combines equipment simplicity, rapid response, and the capability for full-profile reconstruction.

Monitoring methods based on modal evolution and cutoff characteristics offer distinct advantages, including simplicity, real-time capability, and non-destructiveness. However, traditional time-domain optical intensity monitoring methods [28,29] are highly susceptible to environmental noise (e.g., flame turbulence), causing critical cutoff features to be obscured by background noise and hindering precise identification. While existing Short-Time Fourier Transform (STFT) techniques [30,31] operate effectively in low signal-to-noise ratio (SNR) environments, they have not yet introduced active control mechanisms into the fabrication process. Furthermore, a shared limitation among these existing time-domain and frequency-domain methods is that they primarily focus on identifying specific diameter points, remaining limited in their ability to dynamically reconstruct the complete geometric profile of the MNF during the tapering process.

In this paper, we present an experimental platform that employs the interference between higher order mode LP_{02} (HE_{12} in strong guiding regime (SGR)), LP_{11} (HE_{21}, TE_{01}, and TM_{01} in SGR) and fundamental mode LP_{01} (HE_{11} in SGR). Using this scheme and image recognition, MNFs with tailored linear modification factors can be automated fabricated, and their waist diameters can be monitored in real time. Concurrently, we design an end-to-end reconstruction network based on a one-dimensional convolutional neural network (1D-CNN). This network automatically learns the nonlinear mapping between the spatial frequency of intermodal interference signals and the geometric profile of the fiber taper. It enables rapid, high-precision, and direct retrieval of the MNF taper diameter distribution, obviating the need for preset profile functions or complex iterative algorithms. The system demonstrates robust applicability for diameter measurement of MNFs under both adiabatic and non-adiabatic conditions.

2 Theoretical principles

2.1 Calculation formula

In the process of fiber tapering, when the length of the heated zone changes linearly with the tapering distance, the fiber waist diameter follows the condition described in Ref. [32]:

$$D(L)=\begin{cases} D_0 e^{-\frac{L}{2h}}, & (\alpha=0), \\ D_0\left(1+\dfrac{\alpha L}{h}\right)^{-\frac{1}{2\alpha}}, & (\alpha\neq 0), \end{cases} \tag{1}$$

where D_0 represents the initial fiber diameter, h is the initial length of the heated zone, L is the tapering distance, and α is the linear modification factor. Figure 1a illustrates the variation in fiber shape with tapering distance for different linear modification factors, when $\alpha=0$, the fiber diameter decreases exponentially as the taper length increases, and when $\alpha=0.5$, the fiber shape follows a hyperbolic curve.

Taking the tapered fiber with a constant heated region length as an example, the corresponding fiber shape satisfies the prediction model:

$$D(z,L)=\begin{cases} D_0\exp\left(-\dfrac{z}{h}\right), & \left(0<z<\dfrac{L}{2}\right), \\ w\equiv D_0\exp(-L/(2h)), & \left(\dfrac{L}{2}<z<\dfrac{L}{2}+h\right). \end{cases} \tag{2}$$

Here, w is the waist diameter of the tapered fiber, with a length of h, and z is the distance along the fiber axis to the start of the waist region. Typically, when the initial diameter and tapering distance are known, the waist diameter of the fiber is measured using an optical microscope. By substituting this into Eq. (1), the effective heated region length is obtained, which then allows for deriving the waist diameter for each tapering stage. However, the heated region length is not a constant value, slight changes occur during each tapering process, and these variations are the primary source of fiber diameter errors [30]. Thus, to measure more accurately, it is crucial to determine the change in the heated region length after each tapering step, thereby obtaining a more reliable value. To achieve this, modal interference of transmitted light during the tapering process can be used to obtain the fiber diameter at a specific tapering distance, which is then used to correct h.

The propagation of light in a MNF is governed by the Helmholtz equation, in which the propagation constant β and modal fields correspond to the discrete eigenvalues and eigenfunctions under given boundary conditions. As the fiber diameter decreases along the taper region, the boundary conditions vary, resulting in the excitation and cutoff of different modes. For a fixed input wavelength, each mode

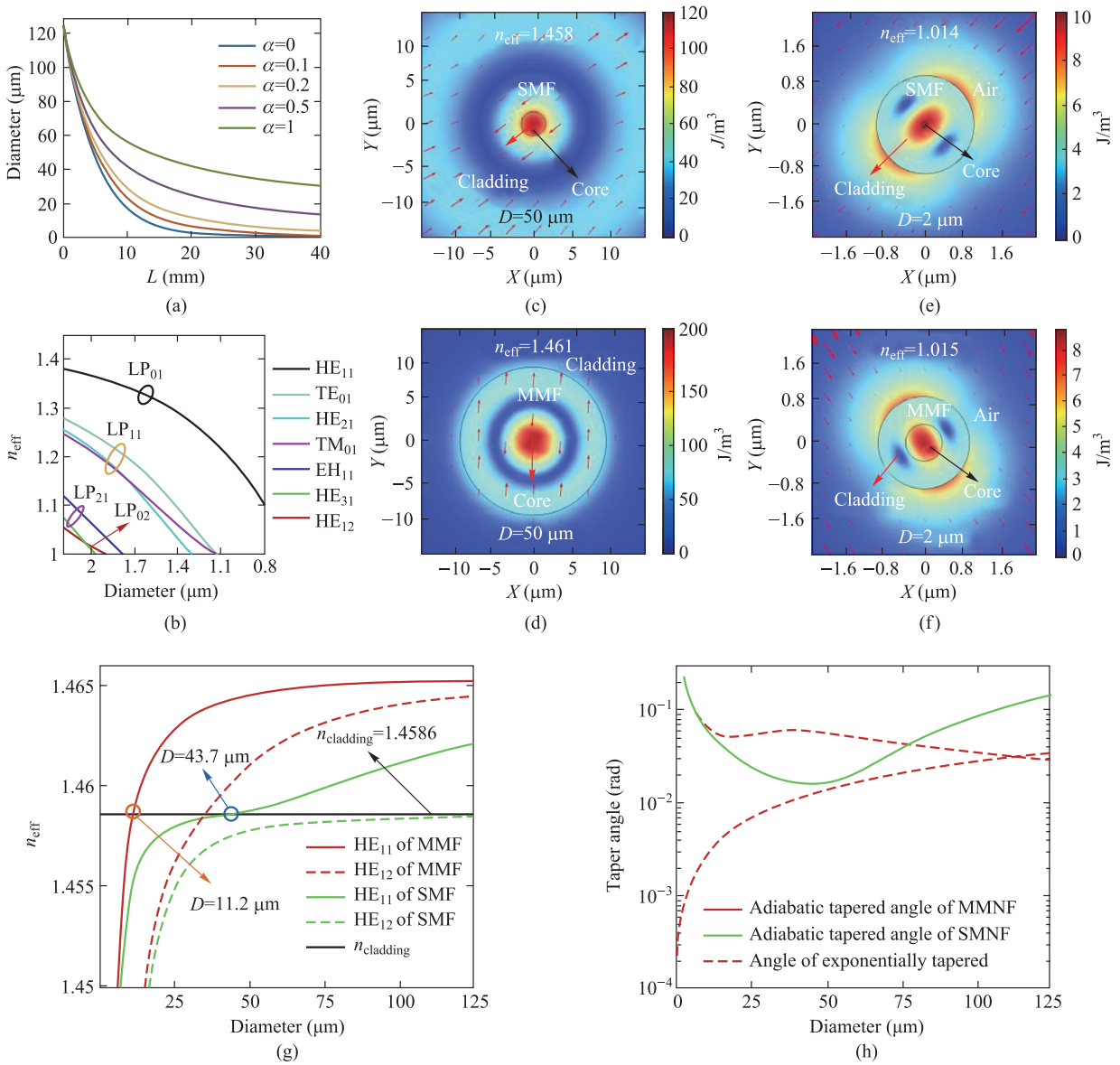

Fig. 1 (a) Fiber shape variation versus taper length for different linear modification factors. (b) Effective refractive indices of selected modes for $\alpha = 0$, showing the decrease of the single-mode fiber (SMF) diameter; modes within the same ellipse are from the same family. (c) and (d) The COMSOL-simulated energy density distributions of the HE_{12} mode for SMF and multimode fiber (MMF) with 50 μm cladding. Red arrows represent the transverse electric field. The simulation used an air–cladding–core three-layer waveguide, with the air layer thickness set to four wavelengths (6.2 μm), and the core diameters set to 0.0656 and 0.4 times the cladding diameter for SMF and MMF, respectively. (e) and (f) Energy density distributions of the HE_{12} mode for SMF and MMF with a cladding diameter of 2 μm under the same simulation conditions. (g) Effective refractive index of HE_{11} and HE_{12} as a function of fiber diameter. Black dashed lines denote the cladding refractive index, while blue and orange circles indicate the diameters at which the HE_{11} leaks into the cladding for SMF and MMF, respectively. (h) Adiabatic conditions of SMNF and MMNF, and the variation of the taper angle with fiber diameter in an exponential-shaped taper region, The *y*-axis is plotted on a logarithmic scale.

possesses a well-defined cutoff diameter D_i that can be determined by solving the eigenvalue equation [33]. During tapering, the cutoff distances L_i of observable modes can be recorded and mapped to their corresponding cutoff diameters. These cutoff distance–mode pairs (L_i, D_i) are then substituted into Eq. (2) to calibrate the hot-zone length h. Because h evolves dynamically with the tapering process, incorporating a greater number of cutoff distance–mode pairs yields higher calibration accuracy.

In the case of tapering with a fixed hot-zone length, the

final waist diameter for $i = 1$ can be expressed as:

$$D = D_0\left(\frac{D_1}{D_0}\right)^{L/L_1}. \tag{3}$$

Here, D_0 corresponds to the initial fiber diameter (125 μm), while L denotes the total pulling length of the taper. Accordingly, the final waist diameter evaluated at reference points $i = 1,2$ is given by:

$$D = D_1\left(\frac{D_1}{D_2}\right)^{(L-L_1)/(L_1-L_2)}. \tag{4}$$

In the case of a taper fabricated with a linearly varying hot-zone, the resulting waist diameter for $i = 1$ can be expressed as:

$$D = D_0\left\{1+\frac{L\left[\left(\frac{D_0}{D_1}\right)^{2\alpha}-1\right]}{L_1}\right\}^{-1/(2\alpha)}. \tag{5}$$

When utilizing a pair of mode cutoffs ($i = 1,2$), the corresponding waist diameter is formulated as:

$$\begin{cases} D = D_1\left(\frac{h+\alpha L_1}{h+\alpha L}\right)^{1/(2\alpha)}, \\ h = \frac{\alpha(L_1-L_2)}{(D_2/D_1)^{2\alpha}-1} - \alpha L_2. \end{cases} \tag{6}$$

Furthermore, to simultaneously correct both parameters h and α, the two corresponding data pairs (L_i, D_i) must be substituted into the following transcendental equation:

$$2\alpha\ln\left(\frac{D_i}{D_0}\right)+\ln\left(1+\frac{\alpha L_i}{h}\right)=0. \tag{7}$$

Solve for the variables (α, h) and substitute them into Eq. (7) to obtain the final waist diameter.

2.2 Discussion of adiabaticity

The single-mode fiber (SMF) employed in this study is Corning SMF-28e, while the multimode fiber (MMF) is of the 50/125 specification. Both fibers have a cladding diameter of 125 μm. The core diameter of the SMF is 8.2 μm, whereas the MMF has a core diameter of 50 μm. Both fibers possess the same core refractive index of 1.4504 [34], with the cladding refractive index calculated as 1.4437 using the Sellmeier formula. Given the high processing temperature of 1423 K, the core and cladding refractive indices are corrected to 1.4654 and 1.4586, respectively, to account for the thermo-optic effect [35,36]. The cutoff diameters of supported modes were obtained by COMSOL simulations at 1550 nm, using a three-layer air–cladding–core model in which the core and cladding diameters varied proportionally while the air thickness remained unchanged. As depicted in Fig. 1b, the effective refractive index n_{eff} of each mode decreases with decreasing fiber diameter, and when $n_{\text{eff}} = n_{\text{air}} = 1$, the mode leaks into the air, defining its cutoff point. The cutoff diameters for modes HE_{31}, EH_{11}, HE_{12}, HE_{21}, TM_{01}, and TE_{01} were found to be 1.780, 1.977, 1.903, 1.296, 1.136, and 1.136 μm, respectively. Experimentally, the interference signal between the fundamental mode and higher-order modes were observed during the tapering process. The disappearance of a given interference signal indicated the cutoff of the corresponding mode, and the taper elongation at that position, combined with the known cutoff diameter, yielded a (L_i, D_i) data pair. However, obtaining multiple pairs of (L_i, D_i) is not always feasible, as it depends on whether the MNF satisfies the adiabatic condition [11,37,38]. In particular, the local tapered angle $\theta(r) = (\mathrm{d}r)/(\mathrm{d}x)$ must be significantly smaller than angle $\Omega(r)$:

$$\Omega(r) = \frac{r\Delta n}{\lambda}. \tag{8}$$

Here, r is the fiber radius, $\Delta n = n_1 - n_2$, n_1, n_2 are the refractive indices of the HE_{11} and HE_{12} mode, respectively, and λ is the wavelength of the light. For a MNF fabricated from a SMF (SMNF), as depicted in Figs. 1c and 1e, the fiber remains single-mode in the wider taper region. The HE_{12} mode exists solely in the cladding, whereas the fundamental mode is located in the core, as seen in Fig. 1g. The significant refractive index difference Δn between these two modes means the adiabatic condition is readily satisfied, according to Eq. (8). When n_1 decreases to that of the cladding (at $D = 43.7$ μm), the HE_{11} mode begins to leak into the cladding and couples with the HE_{12} mode. The smaller Δn in this region makes it challenging to meet the adiabatic condition. As the radius is further reduced, Δn increases again, and the adiabatic condition becomes less stringent. For a MNF created from a MMF (MMNF), also shown in Figs. 1d and 1f, the HE_{12} mode, similar to the fundamental mode, gradually transitions from a core mode to a cladding mode. The overall trend for Δn is an increase (with a slight dip at $D = 11.2$ μm where the fundamental mode becomes a cladding mode), making the adiabatic condition progressively easier to satisfy. However, as illustrated by the red dashed and solid lines in Fig. 1g, the almost identical refractive indices of the two modes at the start of the taper make it difficult to satisfy the adiabatic condition. Figure 1h shows the taper angles that satisfy the adiabatic condition for both types of MNFs. The red dashed line represents the taper angle variation of a natural exponential taper. Its initial intersection with the MMNF's adiabatic curve indicates that the adiabatic condition is not met. In this study, our heat source had a width of approximately 5.1 mm. This process is adiabatic for the SMNF, yielding only a single (L_i, D_i) pair, but it is non-adiabatic

for the MMNF, which allows for multiple (L_i, D_i) pairs to be obtained. Non-adiabatic MNFs produced from SMF are widely used in practical applications. To replicate this situation, we used a two-step tapering method. First, a SMF was tapered to have a long waist and a short taper region. Subsequently, the long waist was tapered a second time. Because a shorter initial diameter requires less tapering length to achieve the same final diameter, the resulting taper angle is larger, which more easily violates the adiabatic condition. A microscopic image of the fiber produced via this two-step tapering method is shown in Fig. 2i. This image is a mosaic of 651 individual pictures, with the transverse and axial directions not being to scale. The fiber has two waist regions with diameters of 55 μm and 8 μm.

2.3 Recognition of modes

The measured light intensity of the interference between the two modes can be expressed as [39]:

$$I = I_i + I_j + 2\sqrt{I_i I_j}\cos\phi_{ij}(L)\cos\theta_{ij}. \tag{9}$$

In this expression, I_i and I_j correspond to the intensities of modes i and j, θ_{ij} is the angle between their polarization states, while ϕ_{ij} denotes the cumulative phase accumulated between the two modes along the fiber owing to differences in refractive index. L represents the total pulling length of the taper, and the accumulated phase can be written as [40]:

$$\phi_{ij}(L) = \int_0^L \left(\beta_i(r(z)) - \beta_j(r(z))\right)\mathrm{d}z. \tag{10}$$

The spatial frequency varies proportionally with the rate of change of the accumulated phase along the tapering length, and can be written as:

$$K_{ij} = \frac{1}{2\pi}\frac{\mathrm{d}\phi_{ij}}{\mathrm{d}L}. \tag{11}$$

Mode cutoffs appear as sudden frequency truncations in the frequency spectrum of the interference signal. By fitting the theoretically computed values to the STFT spectrogram of the interference data, the modes at the cutoff positions can be recognized. The findings show that, in highly adiabatic scenarios, only LP_{02}-LP_{01} interference is observed, while in less adiabatic scenarios, interference between LP_{11} and LP_{02} modes with the LP_{01} mode predominantly occurs.

3 Experimental setup

Figure 2a illustrates the schematic diagram of the experimental setup. A 1550 nm laser source (LS-1550-10 dB-FC/PC-80 MHz) with a linewidth of 0.04 pm is coupled into the optical fiber. To prevent the interference from becoming invisible due to orthogonal polarization states between the coupled modes, a polarization controller (PC) was employed after the light source when drawing SMNFs, thereby ensuring optimal visibility in the STFT spectrograms. The homemade electric heater is regulated by a computer-based temperature feedback system to maintain the fiber at a temperature above 1423 K. When the fiber softens, the translation stages are actuated under program control to pull the fiber symmetrically from both ends. For the constant heat zone heating method, the displacement stage speed is constant at 0.2 mm/s. For the linear heating zone method, the fiber stretching speed remains unchanged, and the displacement stage periodically scans to simulate the increase in the heated area. The movement method follows the approach in references [41–43]. The transmitted light is received at the other end of the fiber after passing through an optical attenuator, by a photodetector (Thorlabs DET08CFC). It is then converted into an electrical signal, displayed, and stored as voltage values by the oscilloscope (Rohde & Schwarz RTO1014). The sampling rate is set to 1 k Sample/s, and the computer processes the received data.

The homemade electric heater [44] is mounted on a vertical stainless steel guide rail (Fig. 2b), while high-precision motorized stages extend the fiber bi-directionally along the vertical axis. To highlight the superior turbulence control of the vertical tapering configuration, we performed SolidWorks Flow Simulation of the gas-flow distribution inside the horizontal and vertical heaters at 1423 K, as presented in Figs. 2c–2f. The results indicate that the horizontal heater exhibits a complex flow pattern with pronounced turbulence near the gas inlets and outlets at the fiber cross-section, whereas the vertical heater maintains a simpler upward flow parallel to the fiber-drawing direction, exerting negligible influence on the fiber profile. This symmetric airflow in our vertical drawing setup effectively suppresses mechanical microbending, and the localized heating (1423 K) intrinsically provides thermal annealing to relieve residual stresses. Consequently, the fiber samples maintain excellent mechanical integrity during both single- and multi-step tapering [44–46]. We further tapered several SMNFs using both horizontal and vertical drawing setups with a target linear modification factor of $\alpha = 0.05$ at lengths of 50 mm. The waist diameters and heated zone lengths of these samples were characterized via SEM, and the actual α values were back-calculated using Eq. (1). The statistical results are summarized in Figs. 2g–2h. While the mean diameters and α values are similar between the two setups, the samples produced with the vertical drawing setup exhibit a markedly narrower distribution for both pa-

rameters, demonstrating improved uniformity.

Following data import, the time–frequency spectrum of the signal is obtained using the STFT with a Hamming window of length 1024 and an overlap length of 960. The use of an ultra-narrow linewidth laser source provides high spectral resolution in the transmission spectrum. By applying image processing to the resulting spectrogram, the cut-off points of the modes can be accurately identified, enabling automated measurement of the MNF diameter. The detailed procedure is as follows: first, the spectrogram is preprocessed (including image enhancement and noise reduction). Then, the connected regions in the image are

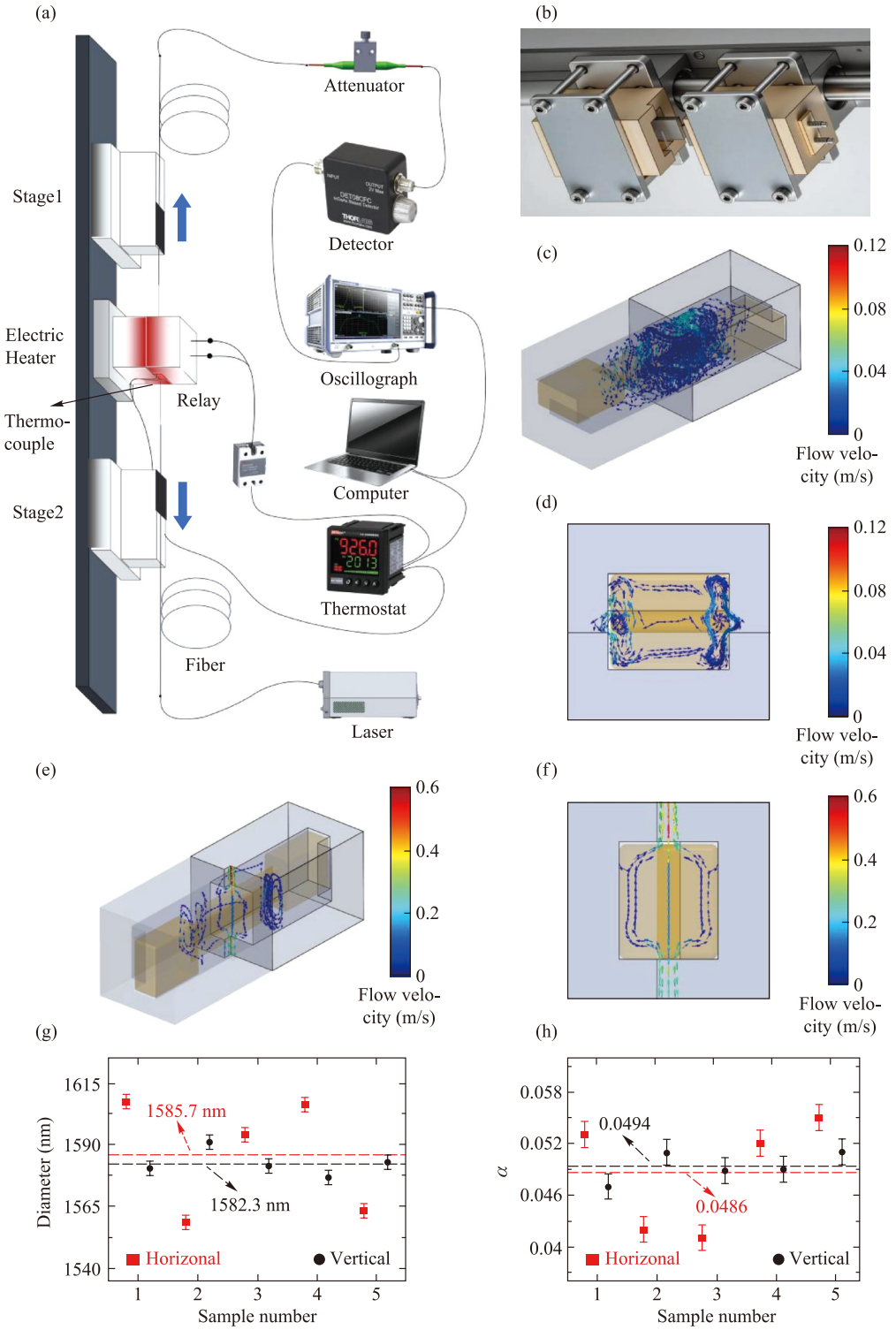

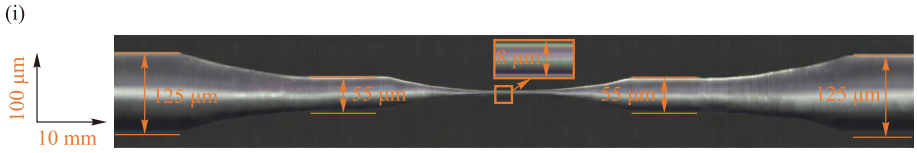

Fig. 2 (a) Experimental setup. (b) Photograph of the vertical electric heater. (c) and (d) Simulated airflow distribution inside the horizontal heater cavity and at the fiber cross section, performed using SolidWorks Flow Simulation. The heater housing is Al_2O_3 (40 × 40 × 65 mm) and the heating element is Si_3N_4, with a set temperature of 1423 K. (e) and (f) Airflow distribution inside the vertical heater cavity and at the fiber cross section under the same conditions. (g) and (h) Comparison of the measured waist diameters (g) and the back-calculated linear modification factors (h) for SMNF samples fabricated using the horizontal (red squares) and vertical (black circles) heating setups. The target parameters were set to a taper length of 50 mm and $\alpha = 0.05$. The vertical setup yields a much narrower standard deviation for both the diameter (5.25 nm vs. 23.48 nm for the horizontal setup) and α (0.0017 vs. 0.0066 for the horizontal setup). Red and black dashed lines represent the mean values for the horizontal and vertical samples, respectively. Error bars are estimated based on the SEM spatial resolution and experimental data. (i) Microscope image of a dual-waist fiber fabricated by the two-step tapering method.

identified, corresponding to the frequency evolution of each interference mode with respect to the fundamental mode over time. Finally, the coordinates of each point in the connected regions are extracted, and their endpoints are determined. Generally, the endpoint is at the far-right of the connected region. To improve robustness, the condition for determining the endpoint is set to $\max(x^2 + y)$.

4 Experimental results

4.1 Specific waist diameter fabrication

To verify the accuracy and robustness of our system for measuring the diameter of MNFs, we set a series of tapering lengths and fabricated MNFs with different shapes (under different linear modification factors $\alpha = 0$ and $\alpha = 0.1$) using both SMFs and MMFs. Typically, SMNFs in our system exhibit highly adiabatic properties. To simulate a broader range of conditions, we also employed a two-step tapering method to fabricate low-adiabatic SMNFs, followed by the same diameter measurement procedure. For the single-step tapering method, the taper lengths were chosen as 46 mm, 50 mm, and 54 mm for $\alpha = 0$; and 50 mm, 60 mm, and 70 mm for $\alpha = 0.1$. For the two-step tapering method, only the $\alpha = 0$ case was considered: the first tapering length was fixed, and the second tapering length was set to 20 mm, 23 mm, and 26 mm. At the end of each tapering process, the recorded transmission signal was processed to identify the cutoff moments of the interference modes, yielding one or more (L_i, D_i) data pairs. According to the predefined value of α and the number of (L_i, D_i) pairs obtained, one of Eq. (3) to Eq. (6) was used to solve for the waist diameter corresponding to the current tapering length.

In Fig. 3a, the upper panel illustrates the transmission of a SMNF fabricated with $\alpha = 0.1$, recorded as a function of time. Because of the small taper angle, the fiber maintains good adiabaticity, with transmission exceeding 94%. The lower panel shows the STFT of the transmission, where the continuous trace corresponds to the frequency evolution of the HE_{12} mode, which cuts off at approximately 122 s. The upper panel of Fig. 3b presents the transmission obtained during the two-step tapering of an SMNF with $\alpha = 0$. The first tapering produces a 4 cm waist with a diameter of 19 μm. In this strong-guiding waist, the modes propagate with significant confinement, so that after the second heating and tapering, the interference frequencies do not originate from zero. The lower panel shows the STFT spectrum of the transmission, where the gap between 200 s and 250 s reflects the cooling and reheating interval. Because the strongly guided higher-order modes in the micro-waist possess large evanescent fields, the two-step tapered devices exhibit extraordinary sensitivity to external environmental changes, making them highly ideal platforms for ultra-sensitive refractive index, temperature, strain, or biochemical sensing [47]. Figures 3c and 3d depict the transmission and corresponding STFT spectrum for MMNF with $\alpha = 0$ and $\alpha = 0.1$, respectively, with the cutoff points of different modes labeled. Figures 3e–3h show the processed STFT spectrum of Figs. 3a–3d, where the red dots denote the detected cutoff positions and the solid lines represent the spatial frequencies of mode–fundamental-mode interference calculated from Eq. (11). In the case of the two-step tapering method, the cutoff times of the HE_{12}, TE_{01}, and TM_{01} modes occur at approximately 37 s, 45 s, and 48 s during the second tapering. For MMNFs fabricated by single-step tapering, the cutoff times of the corresponding modes are listed in Table 1.

The SEM images of the fabricated samples were obtained as references to verify the reliability of the measurement results, as shown in Fig. 4. For highly adiabatic MNFs, the relative error was better than 0.85% (5 nm) in the 588–1449 nm range when $\alpha = 0$, and better than 0.78% (5

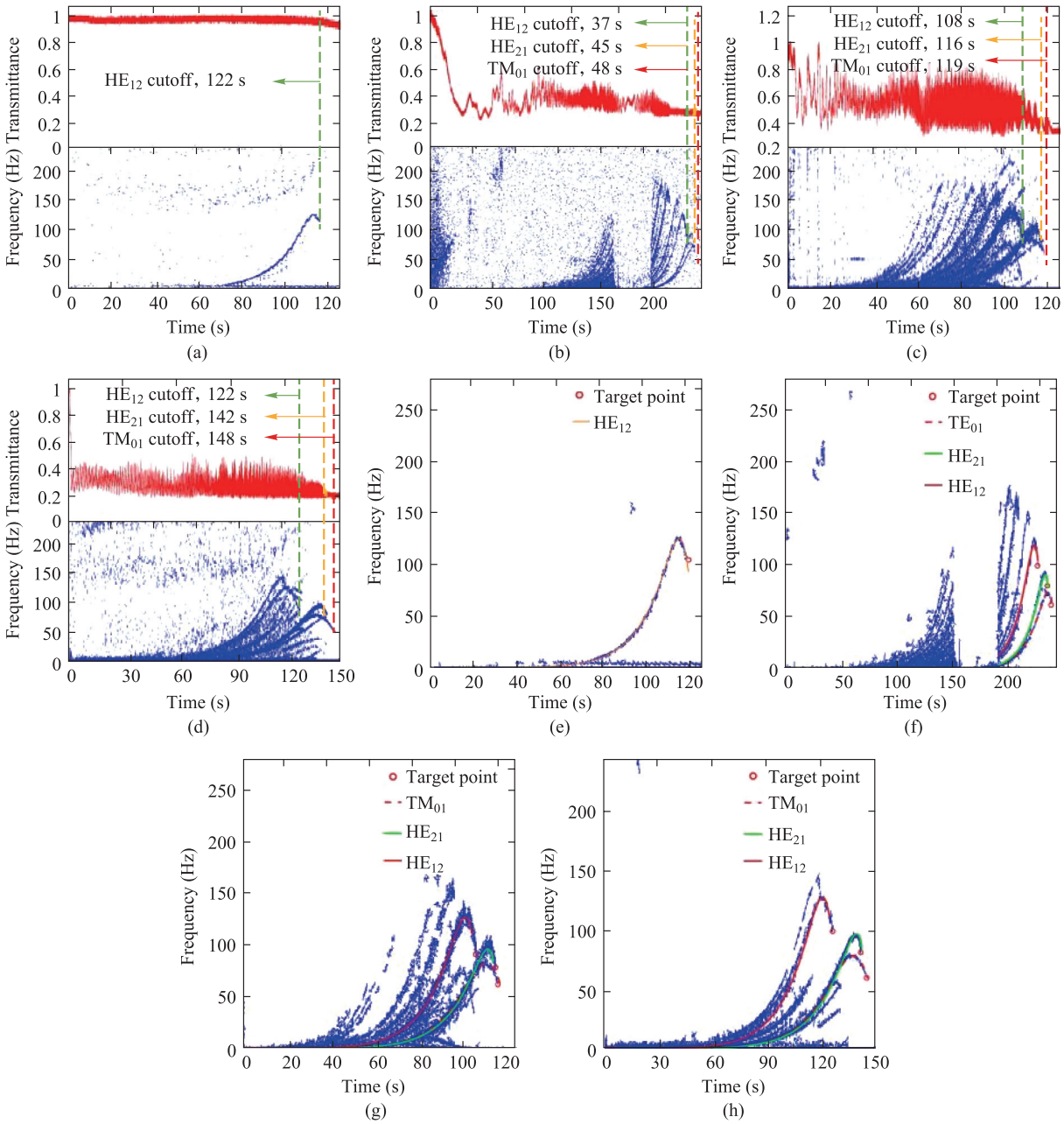

Fig. 3 (a) and (b) Results for SMNFs. Top: Transmission as a function of tapering time for a SMNF with (a): $\alpha = 0.1$ and (b): the two-step tapering method. Bottom: Corresponding spectrograms of the transmission. The dashed lines indicate the cutoff times of individual modes. In (b), the blank region in the spectrogram corresponds to the cooling and reheating process between the two tapering steps. (c) and (d) Results for MMNFs. Upper panels: Transmission evolution versus tapering time for MMNFs fabricated with $\alpha = 0$ and $\alpha = 0.1$, respectively. Lower panels: The associated spectrograms, where the exact mode cutoff moments are delineated by dashed lines. (e)–(h) Processed spectrograms corresponding to panels (a)–(d). The red circles denote the mode cutoff points automatically identified by the program, while the solid lines represent the interference spatial frequencies K_{ij} between the modes and the fundamental mode, calculated according to Eq. (11).

nm) in the 638–1778 nm range when $\alpha = 0.1$. For low-adiabatic MNFs, the relative error was better than 1.14% (7 nm) in the 594–1451 nm range when $\alpha = 0$, and better than 1.25% (8 nm) in the 635–1775 nm range when $\alpha = 0.1$. In addition, for SMNFs fabricated by the two-step tapering method, the relative error was better than 1.14% (6 nm) in

Table 1 Cutoff times of modes under different α (single-step tapering), unit (s)

Mode	$\alpha = 0$	$\alpha = 0.05$	$\alpha = 0.1$
HE_{12}	108	118	122
HE_{21}	116	125	142
TE_{01}	119	128	148

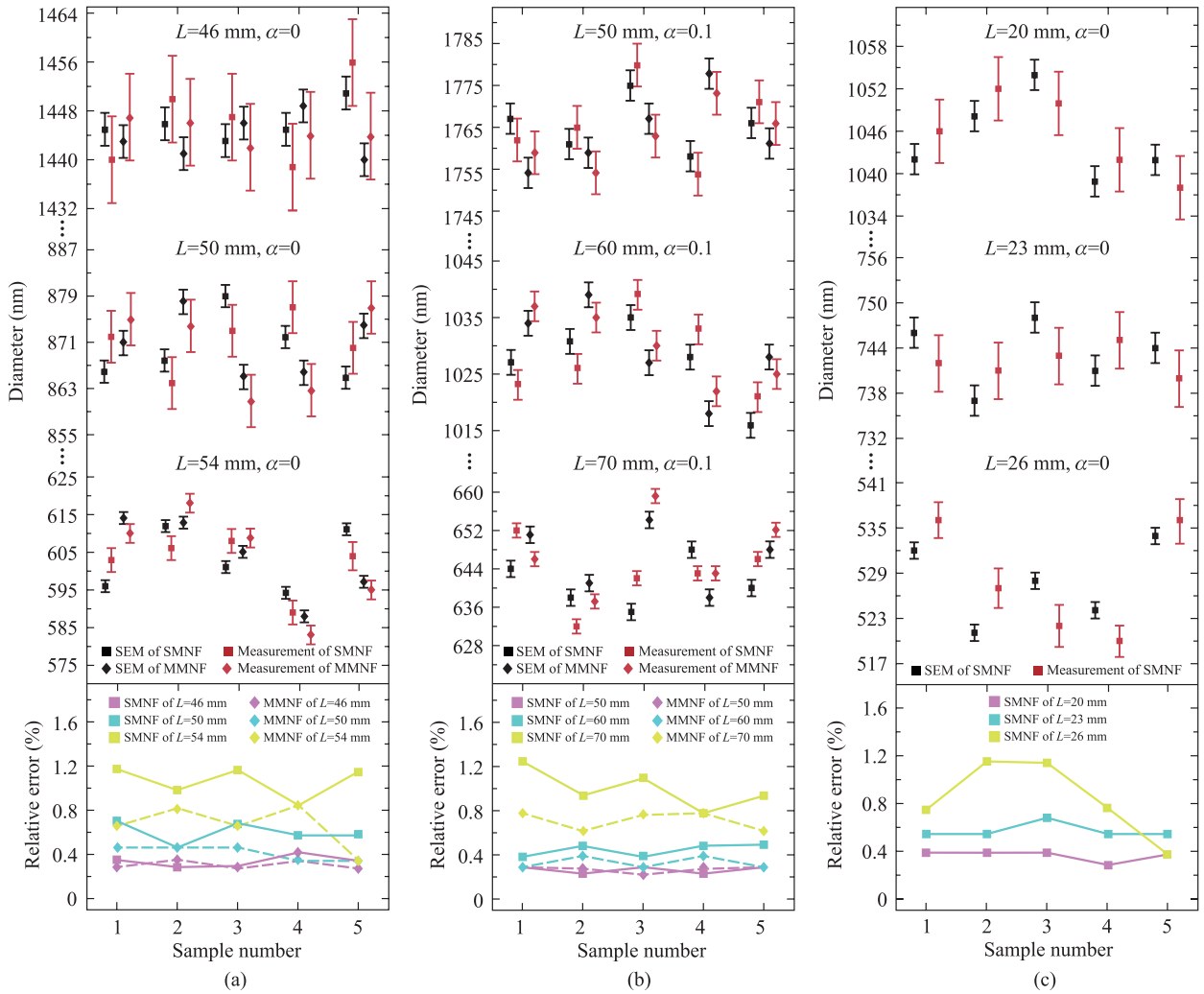

Fig. 4 (a) and (b) Comparison between the measured diameters and SEM results of SMNFs and MMNFs at different preset pulling distances, for $\alpha = 0$ and $\alpha = 0.1$, respectively. Each sample number consists of four data points: SMNFs measurement, SMNFs SEM result, MMNFs measurement, and MMNFs SEM result. (c) Comparison between the measured diameter and SEM results for SMNFs using the two-step tapering method at various pulling distances (only the $\alpha = 0$ case is considered). Each sample number consists of two data points: SMNFs measurement and SMNFs SEM result. The error bars of the red and black shapes are determined by the resolutions of SEM and STFT, respectively.

the 524–1054 nm range. These results clearly demonstrate the high accuracy and robustness of our method for measuring the diameters of MNFs with different taper profiles. This capability provides a reliable technical foundation for the precise fabrication and in situ characterization of MNFs under various tapering conditions.

By integrating the precise measurement capability of our system with a real-time feedback mechanism, we enable the fabrication of MNFs with specific target waist diameters. Fundamentally, this feedback loop operates by translating the on-the-fly detection of a reference mode's physical cutoff into an immediate recalculation of the required remaining tapering length, thereby dynamically updating the motor's target stop position. The specific operational procedure is detailed in Fig. 5. Initially, in the parameter initialization stage, the target waist diameter (D), the linear modification factor (α), and an over-estimated initial pulling distance (L, typically > 70 mm) are preset, and the motorized translation stages start pulling. During tapering, the system enters the Monitoring Module, where the time-dependent optical transmittance is continuously recorded via a custom LabVIEW program. Real-time STFT is applied to map the spatial frequency evolution. Crucially, our image processing algorithm tracks the non-monotonic trajectory of the spatial frequency curve to accurately identify the physical cutoff point of a reference mode. Once the cutoff is successfully detected, the system triggers the Feedback Module. It first extracts the active pulling distance and the corresponding taper diameter (L_i, D_i) at that exact moment. Subsequently, depending on the quantity of

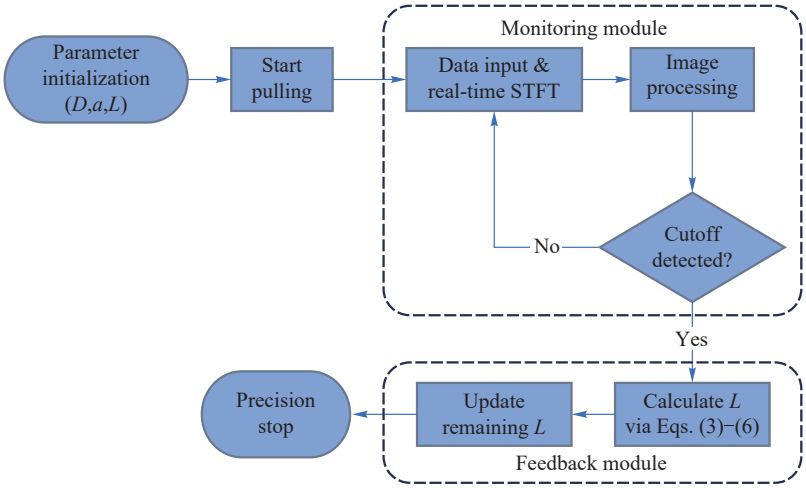

Fig. 5 Schematic diagram of the real-time monitoring and feedback mechanism during the microfiber tapering process.

recorded (L_i, D_i) data points and the preset α, the algorithm calculates the remaining tapering distance required to achieve the final target diameter using the appropriate geometric model from Eq. (3) to Eq. (6). This calculated value is immediately transmitted to the motorized translation stages to update their target stop position. The response time of our system is lower than 10 ms, and due to the relatively slow tapering speed, the error introduced by latency is negligible.

We set the target diameters to 1700 nm, 1200 nm and 700 nm, and fabricated MNFs with three different taper profiles (α = 0, 0.05, and 0.1). After fabrication, the actual diameters were measured using SEM (images are provided in the Supporting Information Figs. S1–S3). The measurement results are presented in Fig. 6: For SMNFs, the maximum relative errors at the preset target diameters were 0.86% (6 nm) under both α=0 and 0.05, and 1% (7 nm) under α=0.1. For MMNFs, these values were 0.57% (4 nm) at α=0, and 0.71% (5 nm) for both α=0.05 and 0.1.

It can be observed that as the target fiber diameter decreases or the linear modification factor increases, the fabrication precision exhibits a slight degradation. This is primarily because a smaller target diameter requires a longer tapering distance, which inherently increases the likelihood of dynamic thermal zone fluctuations over time. This error accumulation can be mitigated by dynamically refining the theoretical calculation formulas based on the measured data to improve accuracy. Furthermore, MMNFs exhibit higher fabrication accuracy at smaller diameters compared to SMNFs. Fundamentally, the excitation of a greater number of higher-order modes in MMNFs provides a higher density of physical reference points during the tapering process. To further improve fabrication precision, the number of excited modes can be actively increased by reducing the incident light wavelength, thereby generating more calibration reference points. In addition, the dynamic measurement accuracy is fundamentally bottlenecked by the inherent time–frequency uncertainty of the STFT method, which introduces a temporal window uncertainty of approximately 0.064 s. This algorithmic limitation can be addressed in future optimizations by adopting multi-resolution analysis techniques, such as the continuous wavelet transform (CWT). Finally, the measurable diameter range is strictly bounded by the physical modal cutoff dynamics. The measurement upper limit corresponds to the fiber diameter at which the first excited mode cuts off (e.g., 1.903 μm for the HE_{12} mode in SMNFs). Conversely, the measurement lower limit extends only to within a few hundred nanometers beyond the final mode cutoff diameter (e.g., 1.136 μm for the TE_{01} mode in MMNFs). Based on waveguide physics, this measurable range can be flexibly tuned: employing a longer incident wavelength increases the measurement upper limit, while adopting a shorter incident wavelength effectively lowers the measurement limit deeper into the sub-wavelength regime.

4.2 Taper profile reconstruction of MNFs based on 1D-CNN

While the STFT cutoff-based method facilitates precise control of the waist diameter, current approaches fail to fully exploit the rich information embedded in the remainder of the time-frequency evolution curve. Equations (10) to Eq. (11) indicate that the intermodal interference trajectory K_{ij} is intrinsically governed by the taper's geometric profile $D(z)$, establishing a deterministic yet complex nonlinear mapping. Consequently, we introduce a 1D-CNN to learn this nonlinear mapping, enabling the direct reconstruction of the taper's geometric profile from the extracted time-frequency curve.

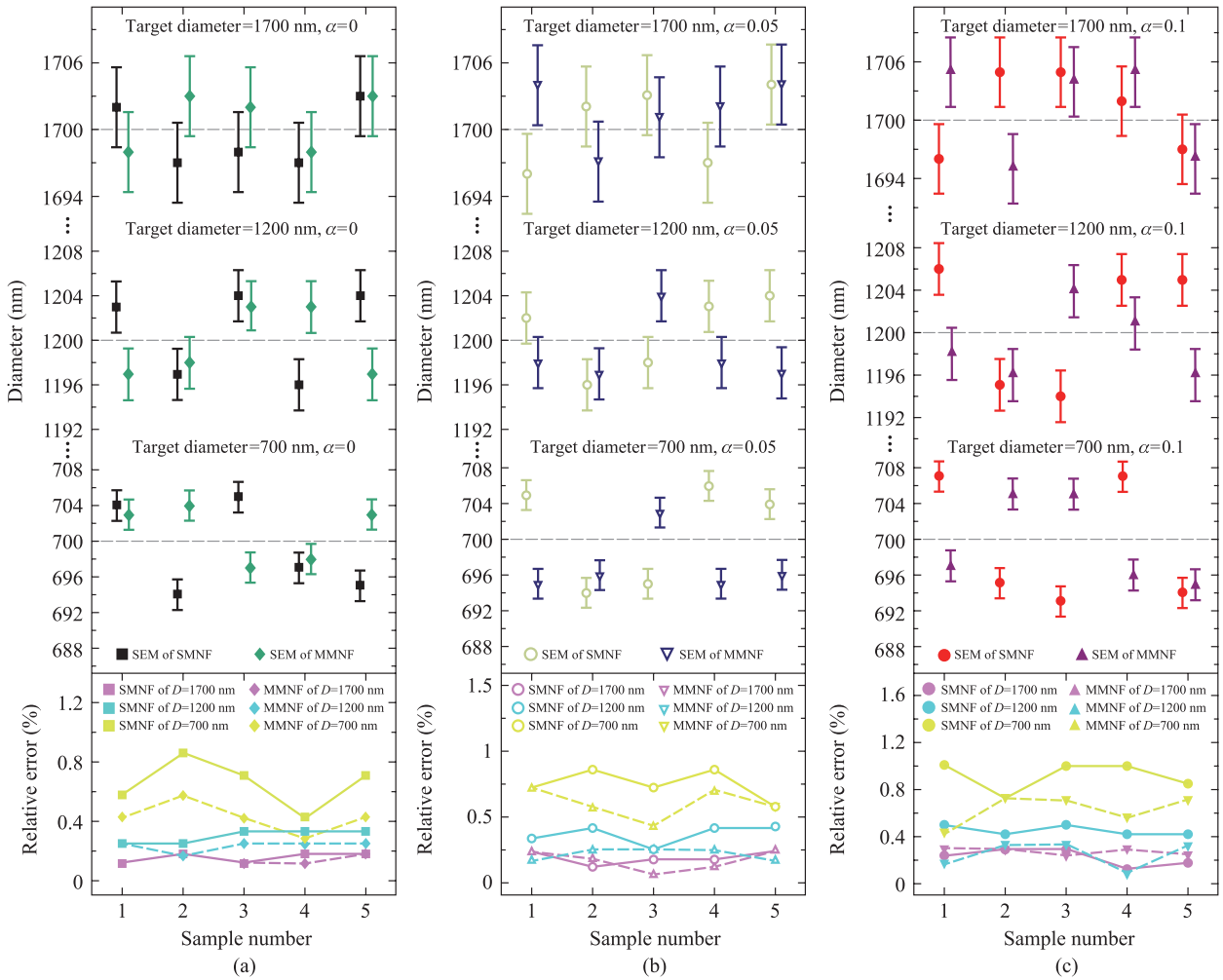

Fig. 6 (a)–(c) Top: SEM-measured diameters of SMNFs and MMNFs when the target waist diameters (black dotted line) are set to 1700 nm, 1200 nm, and 700 nm, for $\alpha = 0$, $\alpha = 0.05$ and $\alpha = 0.1$, respectively. Each sample number consists of two data points: SMNFs SEM result, and MMNFs SEM result. The central data points represent the mean values of 7 spatially distributed diameter measurements (sampled at the thinnest origin and symmetrically at 20 μm intervals along the MNF waist). The error bars indicate the standard error (SE) of these measurements. Bottom: The corresponding relative fabrication errors.

4.2.1 Construction of physics-enhanced data set

The generalization capability of deep learning models is critically dependent on the quality of the training data. Relying solely on theoretical formulas to generate random shape data sets often fails to capture complex process fluctuations inherent in actual tapering, such as airflow perturbations and uneven heating. This discrepancy can lead to model failure when applied to experimental data. To address this, we propose a strategy for constructing a physics-enhanced data set grounded in experimental measurements. We first fabricated 64 MNF samples to serve as data "seeds". These samples included both SMF and MMF precursors, fabricated under the condition $\alpha = 0$, with target pulling lengths distributed across four groups: $L = 37$ mm, 38 mm, 39 mm, and 40 mm, comprising 8 SMNF and 8 MMNF samples per group. Following fabrication, the taper region of each fiber was characterized with high precision using SEM. The axial sampling interval was set to 0.2 mm to acquire authentic discrete profile data.

To transform the discrete SEM measurements into continuous functions suitable for data generation and to augment the data set, we fitted the experimental data using a seventh-order polynomial. This yielded a continuous function describing the fiber diameter D as a function of the axial distance z (measured from the taper transition to the waist), as expressed in Eq. (12):

$$D(z) = A_p \cdot Z\,, \tag{12}$$

where $A_p = (A_0, A_1, A_2, A_3, A_4, A_5, A_6, A_7)$ represents the vector of fitting coefficients, and $Z = (1, z, z^2, z^3, z^4, z^5, z^6, z^7)^{\mathrm{T}}$ denotes the basis function vector. Utilizing the 64 sets

of benchmark coefficients A_p derived from fitting, we introduce minor random perturbations to simulate stochastic process variations inherent to the tapering procedure. Through this data augmentation strategy, each baseline profile generated 2048 simulated samples, thereby constructing a large-scale fiber morphology data set with high physical fidelity.

Subsequently, we employ the physical model (Eq. (11)) to perform forward calculations on each generated profile, yielding the corresponding intermodal interference spatial frequency curves as network inputs. Given that the HE_{12}-HE_{11} interference pattern is stably excited and exhibits distinct features during both SMNF and MMNF tapering, we consistently utilize the interference curve of this mode pair as the feature input. The generated profile data initially consist of 200 axial sampling points. To satisfy the dimensional consistency requirements of the neural network, the input data are uniformly resampled into a (50, 2) tensor comprising the spatial frequency and pulling length dimensions. Retaining the pulling length information assists the network in distinguishing physical states across different tapering stages. Sequences with fewer than 50 points are padded with the maximum frequency value. Similarly, the output labels (profiles) are uniformly resampled into a (50, 1) vector, retaining only the diameter information. In cases of insufficient data length, padding is performed using the minimum diameter value (i.e., the waist diameter). Finally, the constructed physics-enhanced data set is globally shuffled and strictly partitioned into training, validation, and test sets at a ratio of 85%, 10%, and 5%, respectively. This rigorously ensures both the convergence of the model training and the objectivity of the evaluation.

Figure 7 illustrates representative examples of shape perturbations and their corresponding spatial frequency curves used for data set construction. Using two distinct pulling length conditions as examples, Figs. 7a, 7b, 7e, and 7f present the experimentally measured HE_{12}-HE_{11} interference spatial frequency curves and their corresponding taper diameter profiles. The diameter data were acquired via SEM and fitted with polynomials to yield continuous shape functions. The selected pulling length range corresponds to the interval in the spectrogram where the spatial frequency rate of change increases significantly, extending to the HE_{12} cutoff point. Within this interval, the spatial frequency features are distinct and minimally affected by STFT uncertainty, establishing a predictable diameter range of approximately 1.9–10 μm. It is important to note that the actual pulling length covers twice the taper length, a relationship dictated by the axial symmetry of the fabrication process. Building on this, as shown in Figs. 7c and 7g, we generated a set of taper profile samples (D1–D10) distributed around the experimental profile by applying minor perturbations to the fitting coefficients, thereby simulating potential process fluctuations. The corresponding spatial frequency curves, depicted in Figs. 7d and 7h, demonstrate that minute variations in taper geometry induce distinguishable changes in the spatial frequency trajectories while maintaining a consistent overall evolutionary trend.

4.2.2 Neural network architecture design and training strategy

The predictive accuracy and generalization capability of a neural network are critically dependent on the rationality of its architecture and the configuration of its hyperparameters. To establish a high-precision nonlinear mapping from intermodal interference time-frequency features to the fiber taper profile, we constructed a deep 1D-CNN, drawing upon architectural concepts from Ref. [48]. To mitigate the inefficiency of manual parameter tuning, we employed a hyperparameter search strategy inspired by the Hyperband algorithm [49] for the automated selection and optimization of the network architecture and training parameters. This optimization process progressively eliminates underperforming hyperparameter combinations to identify the optimal configuration.

The optimized network architecture is illustrated in Fig. 8. It takes a batch of 32 one-dimensional time-frequency sequences as input, which are first processed by a 16-channel Conv1D layer, followed by a max pooling layer (kernel size 3, stride 2) to extract local time-frequency features and reduce dimensionality. Subsequently, the features undergo Batch Normalization before being input into a second Conv1D layer with 512 channels, followed by another max pooling layer (kernel size 2, stride 2). The features extracted by the convolutional layers are flattened into a 2048-element vector and fed into a regression network comprising four fully connected (FC) layers, each consisting of 2000 neurons. To enhance training stability and mitigate overfitting, Batch Normalization and Dropout layers (with rates of 0.45 and 0.20, respectively) are introduced after the first two FC layers. The final layer serves as the output layer, mapping the network features directly to the physical diameters of the taper profile. Across this architecture, all convolutional and fully connected layers utilize the Rectified Linear Unit (ReLU) activation function, with the kernel size for all Conv1D layers set to 3. The model is trained using the Adam optimizer (learning rate 0.001) to minimize the Smooth L1 loss function, with the threshold parameter set to 4.65.

4.2.3 Neural network test results

To objectively evaluate the generalization performance and

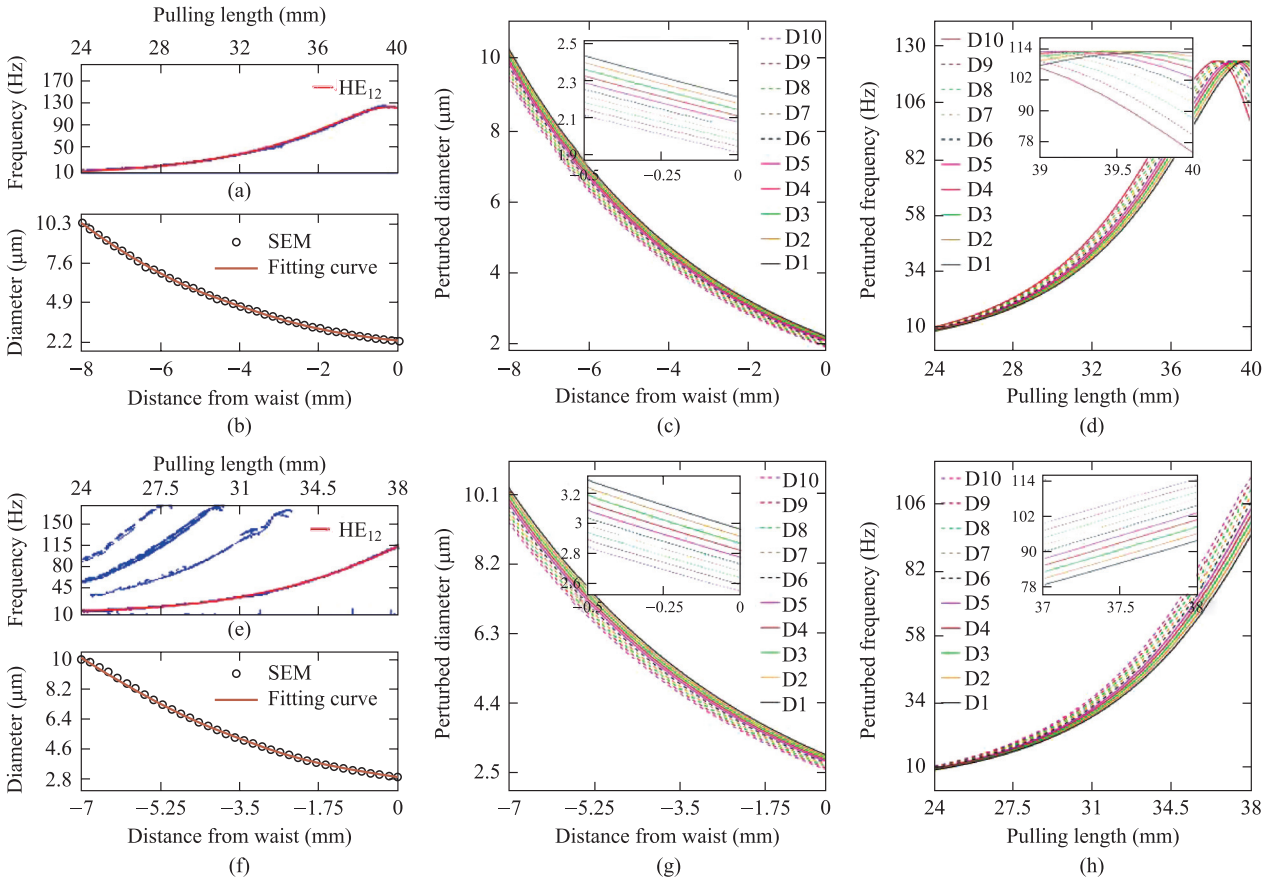

Fig. 7 (a) and (b) HE_{12}-HE_{11} modal interference spatial frequency curves and the corresponding taper profile extracted during SMNF fabrication at a pulling length of $L = 40$ mm. Taper diameters were measured via SEM and fitted using a seventh-order polynomial. (c) and (d) Ten sets of perturbed fiber profiles (D1–D10) generated from the SEM fitting curve, alongside their corresponding spatial frequency curves. For visualization clarity, D1–D10 represent a uniformly spaced subset selected from the augmented data set to clearly illustrate the monotonic physical mapping. Insets show magnified views. (e)–(h) Equivalent analysis applied to MMNF samples at a pulling length of 38 mm. All SEM measurements were conducted at 6k magnification, with a maximum uncertainty of less than 10 nm.

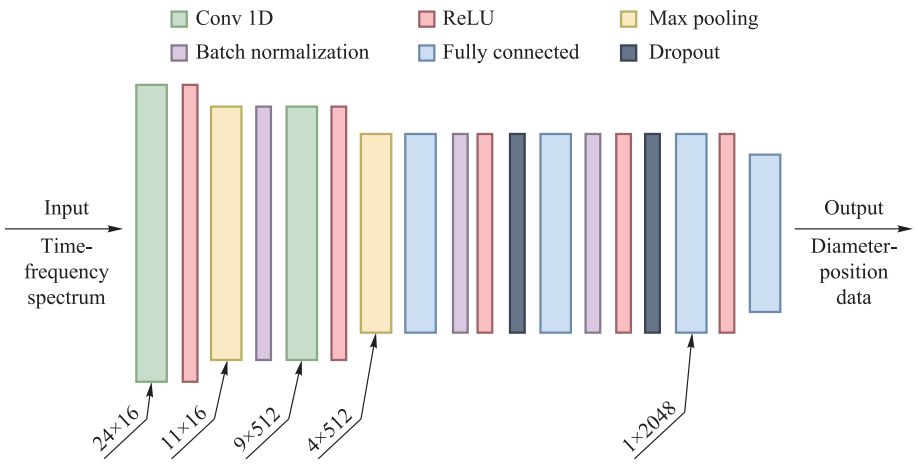

Fig. 8 Neural network architecture following hyperparameter optimization via the Hyperband method. The network accepts the spatial frequency-pulling length spectrum as input and outputs a vector of 50 diameter points corresponding to that specific pulling length. It features two 1D convolutional layers with 16 and 512 channels, respectively, paired with max pooling layers having window sizes of 3 and 2.

measurement accuracy of the trained 1D-CNN model, we constructed an experimental test data set entirely independent of the training set. This test set included both SMF and MMF precursors, deliberately incorporating pulling lengths absent from the training set to assess the model's predictive capability for unseen process conditions. Specifically, MMNFs were fabricated at pulling lengths from 35 mm to 41 mm in 2 mm increments, while SMNFs were fabricated from 36 mm to 42 mm, also in 2 mm increments. Each fabricated sample underwent high-precision SEM profile scanning (0.2 mm interval), covering the taper region from the waist up to a diameter of approximately 10 μm. Subsequently, the HE_{12}-HE_{11} intermodal interference time-frequency evolution curve acquired during fabrication was extracted as the network input. Notably, to align with the network input dimensions and capture the complete stretching history, the input time-frequency curve was cropped to cover the range from the end of tapering back to a point corresponding to twice the SEM measurement span. Feeding the extracted features into the trained 1D-CNN model yielded taper profile predictions, which are compared against SEM measurements in Fig. 9. Across the measurement range, the maximum relative error was less than 0.35%, with the majority of sampling points exhibiting relative errors between 0.1% and 0.2%. The maximum absolute error remained below 9 nm.

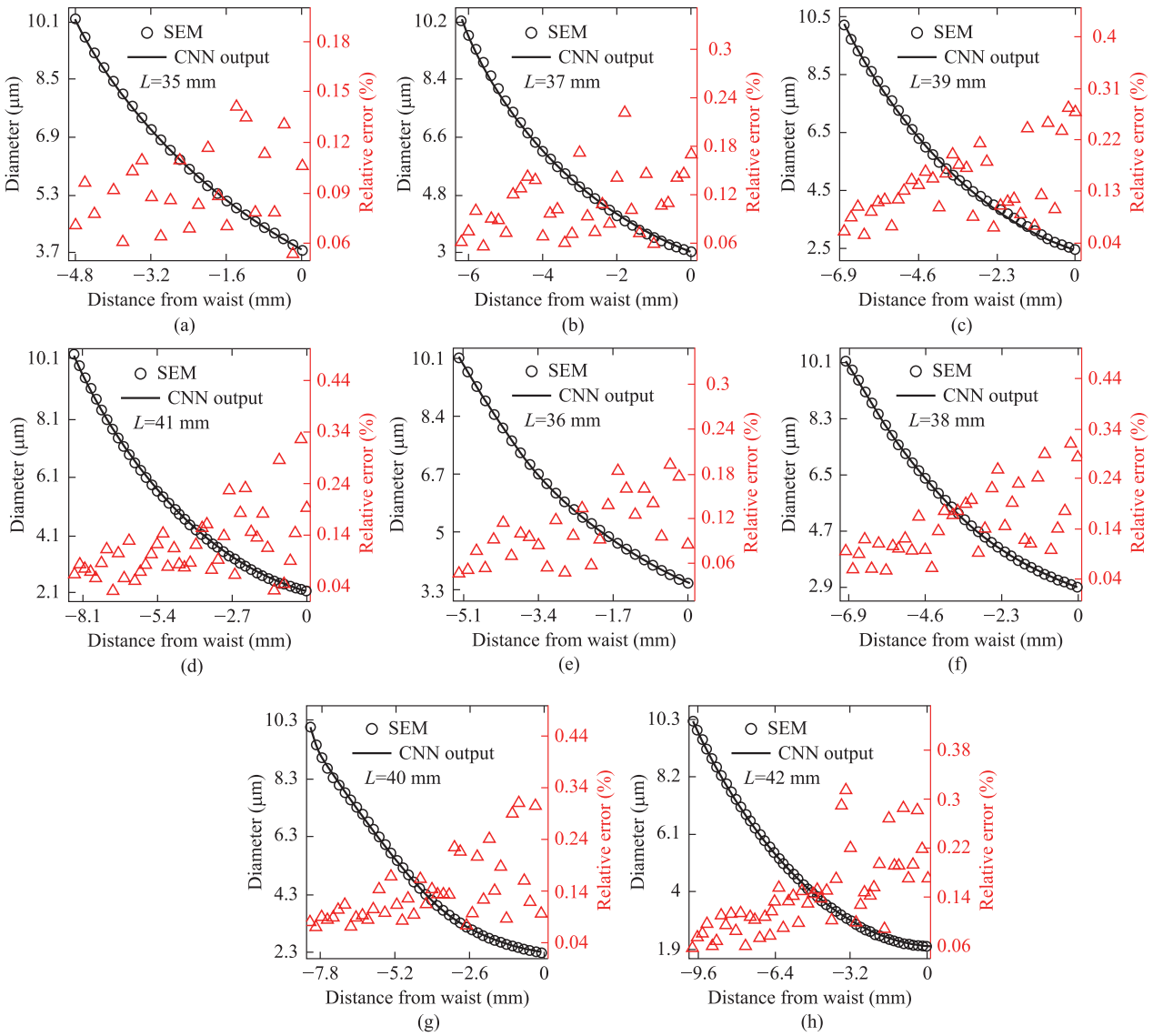

Fig. 9 Experimental prediction results based on the neural network method. (a)–(d) Results for SMNFs. Black circles denote the ground truth profiles, obtained via SEM scanning with an axial step size of 0.2 mm. The measurement span extends from the waist region to the taper section with a diameter of approximately 10 μm. Solid lines represent the network's predicted output, while red triangles indicate the relative error between the predicted and measured values. (e)–(h) Results for MMNFs, following the same analysis protocol as for SMNFs.

These results demonstrate that our 1D-CNN model possesses not only robust nonlinear fitting capabilities but also exceptional generalization performance, enabling high-precision reconstruction of MNF taper profiles under varying pulling conditions. Furthermore, compared to traditional fluid-dynamics and thermo-mechanical models [50,51] that involve complex boundary formulations and iterative solving steps—making them computationally intensive and time-consuming—our method simplifies this process to a direct feed-forward inference and completes the full-profile prediction significantly faster (~5 s). This characteristic provides a practical and efficient alternative for structural evaluation. Additionally, the lower measurement limit can be effectively reduced by training the network on interference patterns involving higher-order modes (e.g., TE_{01}-HE_{11}) or by utilizing a shorter incident wavelength. Conversely, the upper measurement bound can be extended by employing a longer incident wavelength. This methodology is also readily applicable to taper profiles characterized by different linear modification factors. Regarding the neural network input, the spatial resolution of the extracted features is fundamentally constrained by the inherent time-frequency uncertainty of the STFT method. In future iterations, this limitation could be effectively mitigated by adopting advanced time-frequency analysis techniques to extract spatial frequencies with enhanced precision.

5 Conclusion

In conclusion, we have developed a flexible and versatile system capable of rapidly and accurately measuring and fabricating MNFs with various profiles under both adiabatic and non-adiabatic conditions. Our approach innovatively integrates physical model calibration with data-driven strategies. By incorporating a real-time closed-loop feedback mechanism, the system dynamically translates the on-the-fly detection of modal cutoffs into precision motor control. This active monitoring and feedback process facilitates the rapid, non-destructive, and highly deterministic fabrication of MNFs with specific target waist diameters. Concurrently, the 1D-CNN architecture, leveraging spatial frequency data, enables the swift extraction of taper profiles, thereby achieving highly efficient, full-profile MNF reconstruction. This system provides an efficient and reliable manufacturing tool for cutting-edge fields that impose stringent requirements on device precision, such as quantum optics, nonlinear optics, and high-sensitivity sensing.

Supplementary information The online version contains supplementary material available at https://doi.org/10.2738/foe.2026.0022.

Acknowledgements This work was supported by the National Key Research and Development Program of China grant (2023YFF0613000 (YGM)), and the STI 2030-Major Projects grant (2021ZD0200401 (YGM)).

Author contributions DZL and HC carried out experiments. MYJ and JHW helped complete the airflow simulation, and revised the manuscript. YGM and ZNW offered valuable suggestions for the overall conception of the manuscript. YGM supervised the entire project. All authors reviewed and approved the final manuscript.

Declarations

Conflicts of interest The authors declare no conflicts of interest.

Availability of data and materials The data that support the findings of this study are available from the corresponding author, upon reasonable request.

References

1. Tong, L., Lou, J., Mazur, E.: Single-mode guiding properties of subwavelength-diameter silica and silicon wire waveguides. Opt. Express **12**(6), 1025 (2004)
2. Tong, L., Gattass, R.R., Ashcom, J.B., He, S., Lou, J., Shen, M., Maxwell, I., Mazur, E.: Subwavelength-diameter silica wires for low-loss optical wave guiding. Nature **426**(6968), 816–819 (2003)
3. Brambilla, G., Finazzi, V., Richardson, D.J.: Ultra-low-loss optical fiber nanotapers. Opt. Express **12**(10), 2258 (2004)
4. Rusu, M., Herda, R., Kivistö, S., Okhotnikov, O.G.: Fiber taper for dispersion management in a mode-locked ytterbium fiber laser. Opt. Lett. **31**(15), 2257–2259 (2006)
5. Wang, L., Xu, P., Li, Y., Han, J., Guo, X., Cui, Y., Liu, X., Tong, L.: Femtosecond mode-locked fiber laser at 1 μm via optical microfiber dispersion management. Sci. Rep **8**(1), 4732 (2018)
6. Yuan, Y., Yang, P., Peng, X., Cao, Z., Ding, S., Zhang, N., Liu, Z., Zhang, P., Wang, X., Dai, S.: Ultrabroadband and coherent mid-infrared supercontinuum generation in all-normal dispersion Te-based chalcogenide all-solid microstructured fiber. J. Opt. Soc. Am. B **37**(2), 227–232 (2020)
7. Leonov, S.O., Wang, Y., Shiryaev, V.S., Snopatin, G.E., Stepanov, B.S., Plotnichenko, V.G., Vicentini, E., Gambetta, A., Coluccelli, N., Svelto, C., Laporta, P., Galzerano, G.: Coherent mid-infrared supercontinuum generation in tapered suspended-core $As_{39}Se_{61}$ fibers pumped by a few-optical-cycle Cr:ZnSe laser. Opt. Lett. **45**(6), 1346–1349 (2020)
8. Koptev, M.Y., Zaprialov, A.E., Kosolapov, A.F., Denisov, A.N.,

Muravyeva, M.S., Semjonov, S.L., Muravyev, S.V., Kim, A.V.: Visible to mid-IR supercontinuum generation in cascaded PCF-germanate fiber using femtosecond Yb-fiber pump. Fibers (Basel) **11**(9), 72 (2023)
9. Le Kien, F., Balykin, V.I., Hakuta, K.: Atom trap and waveguide using a two-color evanescent light field around a subwavelength-diameter optical fiber. Phys. Rev. A **70**(6), 063403 (2004)
10. Pennetta, R., Blaha, M., Johnson, A., Lechner, D., Schneeweiss, P., Volz, J., Rauschenbeutel, A.: Collective radiative dynamics of an ensemble of cold atoms coupled to an optical waveguide. Phys. Rev. Lett **128**(7), 073601 (2022)
11. Love, J.D., Henry, W.M., Stewart, W.J., Black, R.J., Lacroix, S., Gonthier, F.: Tapered single-mode fibres and devices. Part 1: Adiabaticity criteria. IEE Proc. J Optoelectron. UK. **138** (5), 343 (1991)
12. Ravets, S., Hoffman, J.E., Kordell, P.R., Wong-Campos, J.D., Rolston, S.L., Orozco, L.A.: Intermodal energy transfer in a tapered optical fiber: optimizing transmission. J. Opt. Soc. Am. A Opt. Image Sci. Vis **30**(11), 2361 (2013)
13. Zhang, L., Pan, J., Zhang, Z., Wu, H., Yao, N., Cai, D., Xu, Y., Zhang, J., Sun, G., Wang, L., Geng, W., Jin, W., Fang, W., Di, D., Tong, L.: Ultrasensitive skin-like wearable optical sensors based on glass micro/nanofibers. OEA **3**(3), 190022–190027 (2020)
14. Liang, Z., Wang, C., Tang, Y., Jiang, S., Zhong, X., Zhang, Z., Dai, R.: Non-adiabatically tapered optical fiber humidity sensor with high sensitivity and temperature compensation. Sensors (Basel) **25**(14), 4390 (2025)
15. Liao, B., Li, T., Huang, T., Wang, G., Chen, J., Sun, L., Zhi, Y., Cao, Y., Zhang, J., Li, J., Feng, X., Guan, B.: High-speed organic gas sensor using a microfiber Mach-Zehnder interferometer interrogated based on microwave photonic pulse compression. Opt. Express **33**(9), 18728–18740 (2025)
16. Cen, Q., Pian, S., Liu, X., Tang, Y., He, X., Ma, Y.: Microtaper leaky-mode spectrometer with picometer resolution. eLight **3**(1), 9 (2023)
17. Yalla, R., Sadgrove, M., Nayak, K.P., Hakuta, K.: Cavity quantum electrodynamics on a nanofiber using a composite photonic crystal cavity. Phys. Rev. Lett **113**(14), 143601 (2014)
18. Nayak, K.P., Zhang, P., Hakuta, K.: Optical nanofiber-based photonic crystal cavity. Opt. Lett **39**(2), 232–235 (2014)
19. Sagué, G., Vetsch, E., Alt, W., Meschede, D., Rauschenbeutel, A.: Cold atom physics using ultra-thin optical fibers: light-induced dipole forces and surface interactions. Phys. Rev. Lett **99**(16), 163602 (2007)
20. Vetsch, E., Reitz, D., Sagué, G., Schmidt, R., Dawkins, S.T., Rauschenbeutel, A.: Optical interface created by laser-cooled atoms trapped in the evanescent field surrounding an optical nanofiber. Phys. Rev. Lett **104**(20), 203603 (2010)
21. Spillane, S.M., Pati, G.S., Salit, K., Hall, M., Kumar, P., Beausoleil, R.G., Shahriar, M.S.: Observation of nonlinear optical interactions of ultralow levels of light in a tapered optical nanofiber embedded in a hot rubidium vapor. Phys. Rev. Lett **100**(23), 233602 (2008)
22. Michihata, M., Zheng, Z., Funaiwa, D., Murakami, S., Kadoya, S., Takahashi, S.: In-process diameter measurement technique for micro-optical fiber with standing wave illumination. Nanomanuf. Metrol **4**(1), 28–36 (2021)
23. Hua, Z., Ba, D., Zhou, D., Li, Y., Wang, Y., Bao, X., Dong, Y.: Non-destructive and distributed measurement of optical fiber diameter with nanometer resolution based on coherent forward stimulated Brillouin scattering. Light Adv. Manu. **2**(4), 24 (2021)
24. Liu, Y., Kadoya, S., Michihata, M., Takahashi, S.: Propagation constant-based diameter measurement technique for a submicrometer-scale optical fiber. Opt. Lett **49**(10), 2649 (2024)
25. Michihata, M., Liu, Y., Masui, S., Takahashi, S.: Diameter measurement of nano/micro-optical fiber based on effective refractive index including uncertainty analysis with Monte Carlo simulation. Precis. Eng **97**, 303–316 (2026)
26. Chen, J., Zi, X., Zhang, S., Li, X., Niu, Y., Gong, S.: Real-time measurement and control of nanofiber diameters using a femtowatt photodetector. Opt. Express **30**(7), 12008–12013 (2022)
27. Suman, S., Bashaiah, E., M, R., Yalla, R.: *In situ* characterization of optical micro/nano fibers using scattering loss analysis. J. Appl. Phys **135**(12), 123101 (2024)
28. Xu, Y., Fang, W., Tong, L.: Real-time control of micro/nanofiber waist diameter with ultrahigh accuracy and precision. Opt. Express **25**(9), 10434 (2017)
29. Kang, Y., Gong, J., Xu, Y., Yao, N., Fang, W., Guo, X., Tong, L.: Ultrahigh-precision diameter control of nanofiber using direct mode cutoff feedback. IEEE Photonics Technol. Lett **32**(5), 219–222 (2020)
30. Yu, Y., Zhang, X., Song, Z., Wang, J., Meng, Z.: Precise control of the optical microfiber tapering process based on monitoring of intermodal interference. Appl. Opt., AO. **53**(35), 8222–8228 (2014)
31. Jafari, F., Ranjbar-Naeini, O.R., Zibaii, M.I., Latifi, H.: Profilometry of an optical microfiber based on modal evolution. Opt. Lett **45**(24), 6607 (2020)
32. Birks, T.A., Li, Y.W.: The shape of fiber tapers. J. Lightwave Technol **10**(4), 432–438 (1992)
33. Snyder, A.W., Love, J.: Optical Waveguide Theory. Springer US (1983)
34. Butov, O.V., Golant, K.M., Tomashuk, A.L., Van Stralen, M.J.N., Breuls, A.H.E.: Refractive index dispersion of doped silica for fiber optics. Opt. Commun **213**(4-6), 301–308 (2002)
35. Wang, W., Yu, Y., Geng, Y., Li, X.: Measurements of thermo-optic coefficient of standard single mode fiber in large temperature range. In: Proceedings of International Conference on Optical Instruments and Technology (2015)
36. Rego, G.M.: Temperature dependence of the thermo-optic coefficient of GeO_2-doped silica glass fiber. Sensors (Basel) **24**(15), 4857 (2024)
37. Gonthier, F., Lapierre, J., Veilleux, C., Lacroix, S., Bures, J.: Investigation of power oscillations along tapered monomode fibers. Appl. Opt **26**(3), 444 (1987)
38. Frawley, M.C., Petcu-Colan, A., Truong, V.G., Nic Chormaic, S.: Higher order mode propagation in an optical nanofiber. Opt. Commun **285**(23), 4648–4654 (2012)
39. Salceda-Delgado, G., Monzon-Hernandez, D., Martinez-Rios, A., Cardenas-Sevilla, G.A., Villatoro, J.: Optical microfiber mode interferometer for temperature-independent refractometric sensing. Opt. Lett. **37**(11), 1974–1976 (2012)
40. Ghasemi, P., Yam, S. S. H.: Spectral modal decomposition of abrupt fiber tapers based on simulated annealing method. J. Lightwave Technol. **39**(12), 4209-4216 (2021)
41. Baker, C., Rochette, M.: A generalized heat-brush approach for precise control of the waist profile in fiber tapers. Opt. Mater. Exp **1**(6), 1065–1076 (2011)
42. Ward, J., Maimaiti, A., Le, V., Nic Chormaic, S.: Contributed review: Optical micro- and nanofiber pulling rig. Rev. Sci. Instrum **85**(11), 111501 (2014)
43. Yao, N., Linghu, S., Xu, Y., Zhu, R., Zhou, N., Gu, F., Zhang, L., Fang, W., Ding, W., Tong, L.: Ultra-long subwavelength micro/nanofibers with low loss. IEEE Photonics Technol. Lett **32**(17), 1069–1072 (2020)
44. Chi, H., He, X., Lu, D., Wang, S., Wu, J., Jin, M., Li, X., Wang, Z., Ma, Y.: Precision vertical drawing of diameter-gradient microfibers: cascaded geometries for tailored nonlinearity. Front Optoelectron **18**(1), 16 (2025)
45. Rego, G., Caldas, P., Ivanov, O.V.: Arc-induced long-period fiber gratings at INESC TEC. Part I: Fabrication, characterization and mechanisms of formation. Sensors (Basel) **21**(14), 4914 (2021)
46. Jia, Q., Tang, W., Yan, W., Qiu, M.: Fibre tapering using plasmonic microheaters and deformation-induced pull. Light Adv. Manu. **4**(1), 5 (2023)
47. Taha, B.A., Ali, N., Sapiee, N.M., Fadhel, M.M., Mat Yeh,

R.M., Bachok, N.N., Al Mashhadany, Y., Arsad, N.: Comprehensive review tapered optical fiber configurations for sensing application: trend and challenges. Biosensors (Basel) **11**(8), 253 (2021)
48. Manavi Roodsari, S., Huck-Horvath, A., Freund, S., Zam, A., Rauter, G., Schade, W., Cattin, P.C.: Shape sensing of optical fiber Bragg gratings based on deep learning. Mach. Learn. Sci. Technol **4**(2), 025037 (2023)
49. Li, L., Jamieson, K., Desalvo, G., Rostamizadeh, A., Talwalkar, A.: Hyperband: a novel bandit-based approach to hyperparameter optimization. J. Mach. Learn. Res **18**, 1–52 (2016)
50. Mawardi, A., Pitchumani, R.: Optical fiber drawing process model using an analytical neck-down profile. IEEE Photonics J **2**(4), 620–629 (2010)
51. Yuwono, E.B., Stokes, Y.M., Tronnolone, H., Wylie, J.J.: Coupled heat and fluid transport in pulled extrusion of optical fiber preforms. Phys. Fluids **36**(10), 103129 (2024)

Dezhou Lu is currently a 3nd-year postgraduate student in Prof. Yaoguang Ma's group at State Key Laboratory for Extreme Photonics and Instrumentation, Zhejiang University, China. His research focuses on micro/nano fiber fabrication and its applications.

Hao Chi received his B.S. degree at Xidian University, China, in 2022. He is currently a master student candidate in Prof. Yaoguang Ma's group at State Key Laboratory for Extreme Photonics and Instrumentation, Zhejiang University, China. His research focuses on micro/nano fiber fabrication and its applications.

Liying Chen is an experimental technician (Research Associate) at the School of Optics and Optoelectronics Engineering of Zhejiang University. She graduated from Zhejiang University with a master's degree. Her research focuses on micro-nano optics and nonlinear optics.

Mengyang Jin received his B.S degree at Zhejiang University, China, in 2023. He is currently a master student in the NanoOptics Group of the College of Optical Science and Engineering, Zhejiang University under the supervision of Prof. Yaoguang Ma. His research interests currently center on the automation and multiphysics coupling in the fabrication of optical nanofibers.

Jiahui Wu received his B.S. degree at Zhejiang University, China, in 2023. He is current a graduate student in Prof. Yaoguang Ma's group at State Key Laboratory for Extreme Photonics and Instrumentation, Zhejiang University, China. His research interest is an automated micro nano fiber preparation system.

Zhuning Wang received a B.S. degree from Zhejiang University, Hangzhou, China, in 2020 in optical science and engineering. He is currently at Zhejiang University for the PhD degree. His research mainly focuses on Radiative cooling technology and Micro-nano Optics.

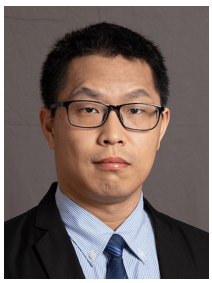

Yaoguang Ma is a Professor at the College of Optical Science and Engineering and deputy dean of Jiaxing Institute, Zhejiang University, China. His research focuses on the study of light-matter interactions at mesoscopic-scale, and micro/nano-techs stem from these interactions for advanced applications in photonic, electronic, and energy systems. His present research focuses encompass metasurface-based devices, computational imaging techniques, precision measurement methodologies, and intelligent sensing systems, spanning interdisciplinary areas that integrate scientific investigation with engineering advancements. In recent years, He have published many highly influential academic papers in international prestigious journals such as Science, PRL, and eLight. with highest single paper citations over 2400.